JOURNAL OF SPACECRAFT AND ROCKETS
Vol. 30, No. 6, November–December 1993

Nonequilibrium Infrared Emission Model for the Wake Flow of Re-Entry Vehicles

Robert L. Sundberg,* James W. Duff,† and Lawrence S. Bernstein‡
Spectral Sciences, Inc., Burlington, Massachusetts 01803

A chemical and thermodynamic nonequilibrium emission model has been applied to the problem of a high-velocity re-entry vehicle. The model consists of a "detailed" state-to-state treatment of the translational-to-vibrational and vibrational-to-vibrational energy transfer processes occurring in a one-dimensional wake flowfield. The resulting nonequilibrium vibrational populations are used to determine vibrational temperatures for the fundamental modes of molecular species. The mode vibrational temperatures are then used to determine approximate vibrational temperatures of hot bands that are used in a rapid, approximate radiative transfer algorithm to predict infrared emission for fundamental and hot-band emission at moderate spectral resolution (5 cm^{-1}). Application of the model to CO_2 4.3-μm band employs a chemical-kinetics mechanism involving 28 CO_2 vibrational states, from which vibrational temperatures of the ν_1, ν_2, and ν_3 fundamental modes are determined. Approximate vibrational temperatures are then determined for 10,000 hot bands that are included in the spectral emission predictions for the 4.3-μm band. Significant nonequilibrium radiation effects are illustrated for CO_2 vibrational bands at 2.7, 4.3, and 15 μm at an altitude of 57.9 km and the 4.3-μm band at 30.5 km.

Nomenclature

C_i = chemical species
C_1 = first radiation constant, 3.741×10^{-12} W cm^2
C_2 = second radiation constant, 1.439 cm K
E_n = vibrational energy of fundamental n, cm^{-1}
E_r = rotational energy of the state, cm^{-1}
E_v = vibrational energy of state , cm^{-1}
g_v = vibrational degeneracy
$I(\nu)$ = monochromatic spectral radiance, $W/sr/cm^2/cm^{-1}$
$k_j(T)$ = temperature-dependent rate constant for the jth energy transfer process
$k_j'(T)$ = temperature-dependent reverse rate constant for the jth energy transfer process
$k_l(\nu)$ = absorption coefficient for the lth emission line, m^{-1}
M = total number of species
N = total number of energy transfer processes
$\bar{R}$ = "effective" source term, $W/sr/cm^2/cm^{-1}$
$\bar{R}_k$ = effective source term for the kth segment, $W/sr/cm^2/cm^{-1}$
$R(\nu)$ = monochromatic emission source term, $W/sr/cm^2/cm^{-1}$
$R_k(\nu)$ = emission source term for the kth segment, $W/sr/cm^2/cm^{-1}$
$R_l(\nu)$ = single-line emission source term for lth line, $W/sr/cm^2/cm^{-1}$
S_k = path-averaged line strength from observer to kth segment, $cm^{-1}/(molec.\ cm^{-2})$
S_l = integrated line strength of the lth line, $cm^{-1}/(molec.\ cm^{-2})$
s = position along the streamline, m
T = flowfield gas temperature, K
T_n = vibrational temperature for fundamental n, K
T_v = vibrational temperature for state, K
u = flowfield velocity along streamline, m/s
u_k = total absorber column density from the observer to the end of the kth segment, $molec./cm^2$
W_D = Doppler single-line equivalent width, cm^{-1}
W_L = Lorentz single-line equivalent width, cm^{-1}
W_l = single-line equivalent width, cm^{-1}
W_V = Voigt single-line equivalent width, cm^{-1}
W_W = weak-line limit equivalent widths, cm^{-1}
X_D = optical depth at center of line, m
α_D = Doppler line width, cm^{-1}
α_k = path-averaged line width from the observer to kth segment, cm^{-1}
α_L = Lorentz line width, cm^{-1}
γ = ratio of the upper-to-lower state rotational vibration populations
$\Delta\nu$ = spectral interval, cm^{-1}
$\bar{\epsilon}$ = spectrally averaged emissivity
$\bar{\epsilon}_k$ = spectral interval averaged emissivity from the observer to start of the kth segment
η_n = number of vibrational quanta in mode n
ν = frequency, cm^{-1}
ν_{ij}' = stoichiometric coefficients for reverse energy transfer process
ν_j = frequency center of the emission line, cm^{-1}
ν_{jj} = stoichiometric coefficients for forward energy transfer process
ρ = flowfield density, $molec./cm^3$
ρ_i = species density, $molec./cm^3$
ρ_v = vibrational state number density, $molec./cm^3$
$\tau_k(\nu)$ = transmittance from the observer to the beginning of the kth segment
$\tau_l(\nu)$ = transmittance for the single emission line
χ_i = mole fraction of ith species, ρ_i/ρ

Subscripts

i = species index
j = energy transfer process index
k, m = segment indices
l = emission line index
n = fundamental mode index

Superscripts

$'$ = upper states
$''$ = lower state

Presented as Paper 92-2916 at the AIAA 27th Thermophysics Conference, Nashville, TN, July 6–8, 1992; received July 18, 1992; revision received Dec. 18, 1992; accepted for publication Dec. 19, 1992.

*Principal Scientist. Member AIAA.
†Principal Scientist.
‡Chief Scientist.

Introduction

THE flight of a high-velocity re-entry vehicle (RV) through the Earth's atmosphere provides an extremely bright and spectrally extensive source of radiation. Quantitative prediction of the emission is of importance for a number of different applications. Examples include prediction of radiative heat loads on vehicle surfaces[1] and evaluation of sensors for locating, tracking, and identifying re-entry vehicles. The focus of the current investigation is on the modeling of the infrared (IR) emission that emanates from the high-temperature gaseous flowfield behind the vehicle. There are two distinguishing features to the current modeling approach: 1) the use of a detailed state-to-state collisional excitation-relaxation model for polyatomic molecules, and 2) the development of a rapid, moderately spectrally resolved (5 cm^{-1}), nonequilibrium IR radiative transfer algorithm for polyatomic molecules.

The emissions arise from a variety of molecular, atomic, and ionic species that are created and excited in the high-temperature flowfield. For nonablatively cooled vehicles, the types of species produced are governed by the chemistry of high-temperature air.[2] For ablatively cooled vehicles, many additional gaseous and particulate species can participate in the chemistry.[1]

The prediction of emission from RV flows is greatly complicated by the nonequilibrium nature of the excitation, de-excitation, and radiative processes. This arises because the collisional excitation and de-excitation processes can occur on a time scale that is slower than that for radiative emission. In such instances, the thermodynamic and radiative properties of the gaseous species cannot be well characterized in terms of a single temperature, the gas-kinetic temperature. Most previous models have treated this problem by using either a two- or three-temperature approximation.[3] In the two-temperature approach, the entire gaseous species mixture is assumed to be described by just two temperatures, one for translational and rotational modes and one for the vibrational and electronic degrees of freedom. In the three-temperature approximation, the vibrational and electronic states are assigned separate temperatures. Some consideration has been given recently to the effect of assigning different vibrational temperatures to the diatomic species present in hot air. These approaches have worked well for their intended application, prediction of the maximum radiative heat loads on vehicle surfaces, where the emphasis is on the emission in the visible and ultraviolet spectral regions. For such cases, the predicted radiative-heat loads are not too sensitive to the exact distribution of vibrational excited states, and thus a simple, global characterization by a single effective vibrational temperature is adequate.

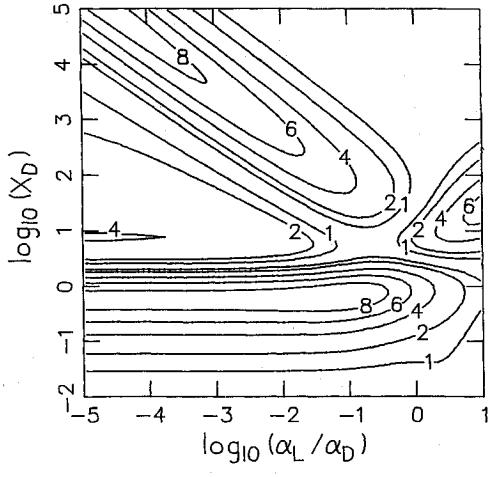

Fig. 1 Absolute value error contours for Voigt equivalent width approximation.

However, the prediction of IR spectral emissions depends strongly on the detailed vibrational excited state distribution for each diatomic and polyatomic species.

The computational approach discussed here involves several steps. First, the bulk flowfield properties, such as the gas-kinetic temperature, pressure, and species concentration are calculated using an appropriate flowfield model.[4] For the sample calculations presented later, a one-dimensional wake flowfield model was employed. Second, the "detailed" vibrational state populations for each molecular species are determined by overlaying a chemical-kinetics calculation on the bulk flowfield properties. Although the population of each vibrational state is determined, only the vibrational populations of the fundamentals and ground state are explicitly used in the emission calculation. Approximate vibrational temperatures are determined for hot bands from the vibrational temperatures of the fundamentals. Finally, the spectral emission along an arbitrary flowfield line of sight (LOS) is computed using a novel nonequilibrium radiative transfer algorithm.[5]

The most accurate method for performing radiative transfer calculations is to use a line-by-line approach, where each emission-absorption line is explicitly considered and a very fine spectral grid is used to resolve the line shape of each vibrational-rotational line. This approach is infrequently used because it involves a relatively large computational effort. A typically stressing calculation was done for the Jupiter Galileo probe and involved upwards of 100,000 lines for diatomic ultraviolet-visible (UV-VIS) emitters.[1] The situation is even worse in the IR for polyatomic molecules, where, for example, at a moderate re-entry temperature of 5000 K approximately 2×10^6 CO_2 lines contribute to the spectral emission.

A rapid radiative transfer approach[5] has been developed that involves three simplifications over the more exact line-by-line method. These simplifications are the following: 1) the spectrally integrated emission for each line is rapidly evaluated using an analytical approximation to its equivalent width, 2) the effect of line overlap is estimated using a statistically based approximation formula, and 3) a band shape symmetry approximation is used to rapidly scale the contribution of hot band lines from their corresponding fundamental band counterparts. The cumulative effect of these approximations is to enable an approximately 10,000-fold increase in computational efficiency over the line-by-line approach, while maintaining errors of less than 10%.

Chemical-Kinetics Overlay Model and Rate Equations

The computation of the spectral radiance from a given species requires that a set of vibrational populations (or, equivalently, vibrational temperatures) be provided as input to the radiation transport model. In the equilibrium limit, the vibrational temperatures are simply given by the gas-kinetic temperature computed by the flowfield model. However, when the time scale for radiative relaxation is comparable to that for collisional excitation and de-excitation, nonequilibrium conditions exist. Under these conditions, the vibrational temperatures are obtained by solving a set of rate equations for an assumed chemical-kinetics mechanism in conjunction with the flowfield model. This procedure can be quite cumbersome if many vibrational states are required for an adequate description of the energy transfer process. In addition, the rate equations describing energy transfer processes often tend to be stiff,[6] requiring a somewhat robust numerical integration scheme.

The solution of the coupled chemical-kinetics/flowfield model can be simplified tremendously by realizing that the infrared radiation results from minor species such as CO_2, CO, and NO, as well as other ablation products. Under the conditions that the energy transfer processes involving minor species in the flow do not influence the macroscopic flowfield properties (such as temperature, velocity, and density), the flowfield solution can be uncoupled from the chemical kinetics involving minor species. An appropriate flowfield model

can first be used to obtain the gas temperature, velocity, density, and species mole fractions along flowfield streamlines. The vibrational populations are then obtained by solving the chemical-kinetics rate equations along the flowfield streamlines for the previously computed flow properties; i.e., the solution to the rate equations is overlaid on the flowfield. This procedure allows the implementation of complex chemical kinetics mechanisms and flowfield models that may be necessary for a realistic treatment of vibrational energy transfer in re-entry vehicle flowfields.

The vibrational energy transfer mechanism involving M species (which may or may not possess vibrational states) participating in N energy transfer processes can be written as

$$\sum_{i=1}^{M} \nu_{ij} C_i \rightleftharpoons \sum_{i=1}^{M} \nu_{ij}' C_i \qquad j = 1, \ldots, N \tag{1}$$

Note that the ν_{ij} and ν_{ij}' are integer coefficients, and since there are typically only a few species participating in any given energy transfer process, the ν_{ij} and ν_{ij}' matrices are quite sparse. The rate equation for the mole fraction of species i, χ_i, corresponding to Eq. (1) is given by

$$\rho u \frac{d\chi_i}{ds} = \sum_{j=1}^{N} (\nu_{ij}' - \nu_{ij}) \left[k_j(T) \prod_{i=1}^{M} \rho_i^{\nu_{ij}} - \kappa_j'(T) \prod_{i-1}^{M} \rho_i^{\nu_{ij}'} \right] \tag{2}$$

The dependence of ρ, u, T, ρ_i, and χ_i on streamline position s has been suppressed. The rate constant $k_j(T)$ for the jth energy transfer process depends only on the gas temperature and thus on streamline position. The reverse rate constant $k_j'(T)$ is related to $k_j(T)$ by microscopic reversibility. Each coupled differential equation represents the rate of energy transfer for species along the flowfield streamline. The vibrational populations are obtained by solving Eq. (2) given the flowfield properties and initial mole fractions using a numerical algorithm[7] based on Gear's method.[6] A vibrational temperature for each state can be defined based on the fraction of molecules in the vibrational state and the energy of that state.

Radiation Transport Model

Computation of the nonequilibrium spectral radiance for a LOS through an RV flowfield requires detailed information about the flow, including gas-kinetic temperature, pressure, species column densities, and either vibrational temperatures or vibrational populations. The flowfield properties are determined for a finite number of stations along the LOS, and the LOS is represented as series of homogeneous segments. For n homogeneous segments the exact monochromatic spectral radiance is given by

$$I(\nu) = \sum_{k=1}^{n} R_k(\nu)[\tau_k(\nu) - \tau_{k+1}(\nu)] \tag{3}$$

Equation (3) is valid for both equilibrium and nonequilibrium conditions, but different computational techniques are normally used for determining the emission source term and transmittance in the two limits.

An approximate, spectrally averaged LOS radiance is obtained by replacing the emission source term in Eq. (3) with an "effective" emission source term that is a slowly varying function of the frequency and by integrating over a narrow spectral interval of width $\Delta\nu$. This results in the equation

$$\langle I \rangle = \sum_{k}^{n} \bar{R}_k(\bar{\epsilon}_{k+1} - \bar{\epsilon}_k) \tag{4}$$

Our approach for determining the source term and average emissivity for a nonequilibrium gas is discussed later.

Emission Source Term

The exact monochromatic emission source term for a homogeneous, nonequilibrium gas is given by

$$R(\nu) = \sum_{l} R_l(\nu) k_l(\nu) / \sum_{l} k_l(\nu) \tag{5}$$

where the sum extends over all emission lines. The nonequilibrium nature of the gas results from the fact that each of the emission lines may have a different source term. The single-line source term is given by

$$R_l(\nu) = \frac{C\nu^3}{\pi} \frac{\gamma_l}{1 - \gamma_l} \tag{6}$$

The population ratio for each emission line includes degeneracy factors and is given by

$$\gamma = g_{v''} \rho_{v'} / g_{v'} \rho_{v''} \exp[-C_2(E_{r'} - E_{r''})/T] \tag{7}$$

The exponential term represents the thermal populations of the rotational states, and so their explicit populations are replaced by a Boltzmann distribution. In the equilibrium limit, the vibrational populations, as well as the rotational populations, are given by a thermal Boltzmann distribution and the single-line emission source function, Eq. (6), converts to the Planck blackbody radiation function.

The exact nonequilibrium source term in Eq. (5) is replaced with an effective source term that is a slowly varying function of frequency, which allows the source term to be removed from the spectral averaging integral that was used to obtain Eq. (4). The effective source term is obtained by replacing the absorption coefficient in Eq. (5) with the spectrally integrated line absorption and by evaluating the single-line source function at the center of the emission line ν_j. The effective source term is then given by

$$\bar{R} = \sum_{j} R_j(\nu_j) S_j / \sum_{j} S_j \tag{8}$$

and the sum is over the lines contained in the interval $\Delta\nu$.

Spectrally Averaged Emissivity

The spectrally averaged emissivity for an ensemble-averaged set of emission lines, where the distribution of line positions is assumed to be uniform across the spectral interval $\Delta\nu$ and there is no correlation between line positions, is given by

$$\bar{\epsilon} = 1 - \prod_{l} \left(1 - \frac{W_l}{\Delta\nu} \right) \tag{9}$$

where W_l is defined by

$$W_l = \int_{\Delta\nu} d\nu[1 - \tau_j(\nu)] \tag{10}$$

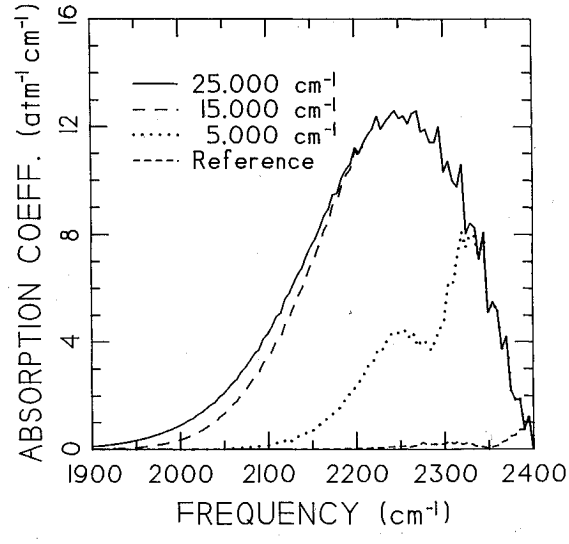

Fig. 2 Dependence of the CO_2 4.3-μm spectral absorption coefficients at 3000 K on the maximum vibrational energy.

Equation (9) includes the effect of line overlap and is similar to the average emissivity expression obtained by Plass for a statistical band.[8] The only difference in the expressions results from Plass's assumption that the line strengths, along with positions, are randomly picked from a normalized distribution. The known line strength distribution is used in the present formulation.

Single-Line Equivalent Width

For the conditions encountered in RV wake flowfields, the emission lines can vary from a pressure-broadened Lorentz to a Doppler line shape, and so a mixed line shape (Voigt) must be used. The Voigt line shape is simply a convolution of the Lorentz and Doppler shapes. The most accurate technique used in calculating the Voigt equivalent width is direct numerical integration.[9] This technique is quite time consuming and therefore impractical for modeling RV wake signatures because millions of rotational vibration lines are expected to contribute to the emission.

Several computationally rapid approximations for the Voigt single-line equivalent width have appeared in the literature. The approximations either replace the Voigt line shape with an approximate line shape that allows for analytic solutions[10,11] or interpolates between the Doppler and Lorentz equivalent widths to obtain an approximate Voigt equivalent width.[12,13]

Rodgers and Williams[12] have suggested an interpolation formula for the Voigt equivalent width given by

$$W_v = \sqrt{[W_L^2 + W_D^2 - (W_L W_D / W_W)^2]} \tag{11}$$

This formula has been shown to give peak errors of 8%. This approximation can be improved to have peak errors of about 1% by using the correction factors developed by Oinas.[13] However, additional computer time is required to calculate the correction factors. Since computational speed is a major consideration for our model, the approximation given in Eq. (11) is used without correction.

Equation (11) requires the Lorentz, Doppler, and weak-line limit equivalent widths. There are accurate expansions that can calculate the Lorentz and Doppler equivalent widths with maximum relative errors of 5×10^{-6},[12] but since the Voigt approximation has peak errors of 8%, more rapid and less accurate approximations can be used to calculate W_L and W_D.[14] In Fig. 1 we show the percent error of the previous approximation when compared with "exact" numerical Voigt equivalent widths. The percent error is shown as a function of the optical depth at the center of a line X_D and the ratio of the

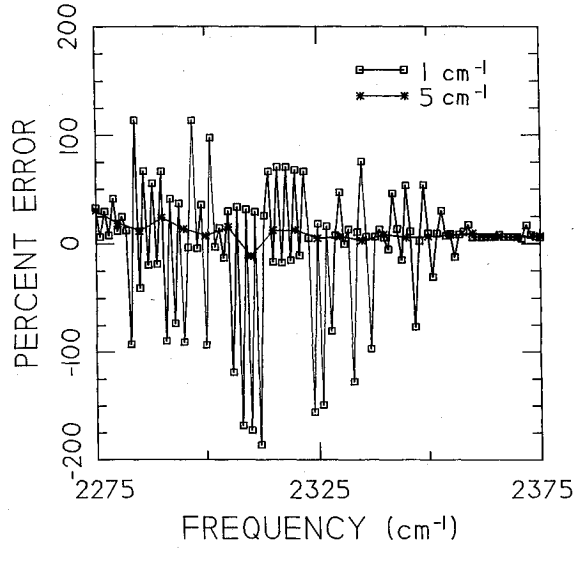

Fig. 3 Percent error in absorption coefficient of CO_2 at 500 K using approximate emission lines at 1 and 5 cm^{-1} resolutions.

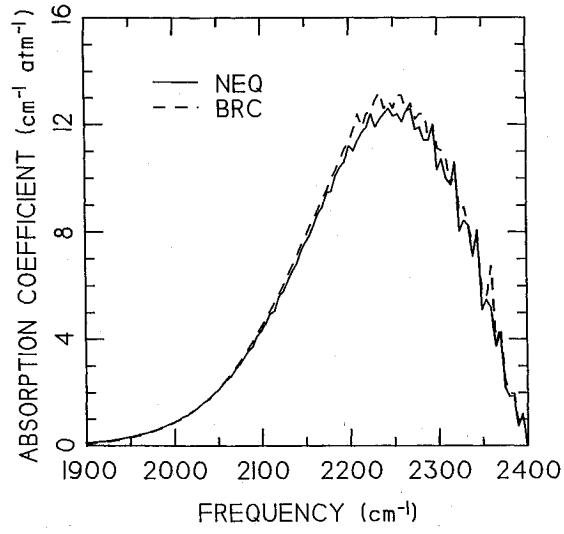

Fig. 4 Comparison of 4.3-μm CO_2 spectral absorption coefficients using approximate emission lines and the model by Bernstein et al.

Lorentz-to-Doppler line widths. These two parameters determine the value of W_V. The peak error for this formulation is less than 10%.

To simplify the equivalent width evaluation for a multisegmented LOS, the Curtis-Godson approximation[15,16] is used to define a path-averaged homogeneous path from the observer to the current homogeneous segment. The path-averaged line strength and line width from the observer to the end of the kth segment are given by

$$S_k = \frac{1}{u_k} \sum_{m=1}^{k} S_m u_m \tag{12}$$

and

$$\alpha_k = \frac{1}{S_k u_k} \sum_{m=1}^{k} S_m u_m \alpha_m \tag{13}$$

where α refers to α_D or α_L.

Emission Line Approximation

The radiation transport model developed in this paper is based on the calculation of single-line equivalent widths for each molecular emission line. To perform these calculations, the necessary emission line information must be tabulated in a data base. The data base must contain line strengths, line widths, and vibrational and rotational energies of the lower state involved in the transition. These parameters are necessary to calculate the temperature-dependent lines' strengths and widths along the optical path. Standard absorption line compilations, such as the HITRAN atmospheric line parameter compilation,[17] have been generated for atmospheric conditions. Therefore, they generally include rotational and vibrational transitions that are important at relatively low temperatures found in the atmosphere (less than 800 K). There are an enormous number of lines that are important at high temperatures that are missing from these compilations. Since these lines must be included to adequately simulate high-temperature wake flowfield emission, theoretical models that have constants derived from low-temperature spectral measurements are used to generate the necessary information. For linear molecules, like CO_2 or diatomics, it is a straightforward procedure to augment the line data base using well-known transition energy and line strength formulas, for example, see Bernstein.[18] For nonlinear molecules, like H_2O, one can use existing asymmetric top codes to predict higher lying transitions and strengths.[19] Since the spectroscopic constants used in generating these lines are based on low temperature measure-

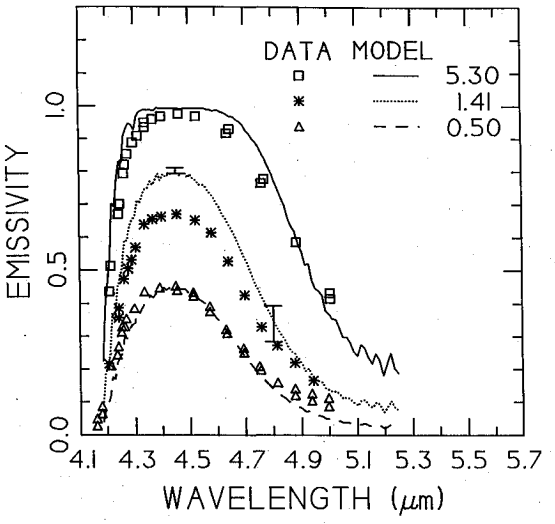

Fig. 5 Calculated and observed spectral emissivities from measurements of Coppalle and Vervisch for three optical densities (atm cm). The calculations are shown as lines, observed data as symbols. Calculated error bars are shown for the intermediate optical density using quoted experimental uncertainties.

Table 1 Inputs for model calculations

Optical density, atm · cm	Length, cm	Temperature, K	X_{CO_2}	X_{CO}	X_{H_2O}
0.5	2.0	2900	0.25	0.10	0.58
1.41	6.8	2900	0.21	0.12	0.58
5.3	21.2	2900	0.25	0.10	0.58

[a]Pressure of 1 atm for all optical densities.

ments, the calculated high-temperature lines suffer from maximum errors in the emission frequency of approximately 5 cm^{-1} and a strength error of 15%.

However, calculation of all of the necessary rotational-vibration lines for a polyatomic molecule would be very time consuming and approximate, since spectroscopic constants required for accurate line position and strength determination exist for only a few of the low-lying bands. This means that some approximate set of constants would be used for the thousands of hot bands for which accurate constants are unknown. Another approach that has been used to determine line positions and strengths for hot bands is to assume that the ro-vibrational lines of hot bands have the same structure and intensity distribution as the fundamental band.[5,20,21] This allows approximate hot band parameters to be determined by shifting and scaling the fundamental's set of lines. Bernstein has pointed out that this approximation should apply only to bands of the same symmetry type, since the band contours for modes of different symmetry generally exhibit significant differences.[21] The use of shifted and scaled fundamental bands to represent the hot bands limits the spectral resolution of our model to 5 cm^{-1}. An important advantage to using this approximation is that the required data base is reduced to storage of the fundamental set of lines (a few hundred) and a "bands" file that contains the hot band locations, degeneracies, and their strengths relative to the reference band. There is also some computational advantage in using this approach because several path-related variables, like the Curtis-Godson averaged line strengths and widths, can be reused for each hot band.

Figure 2 shows the effect of adding additional hot bands to the high-temperature absorption coefficient of CO_2 in the 4.3-μm spectral region. The absorption coefficient is computed, considering all vibrational transitions up to a maximum lower state vibrational energy of E_{max}. The figure shows plots for E_{max} of 5000, 15,000, and 25,000 cm^{-1}, along with the reference band. The emission bands included belong to the transition sequence $(n_1n_2ln_3x) \rightarrow (n_1n_2ln_3 + 1x)$. The notation for the vibrational states $(n_1n_2ln_3x)$ is standard HITRAN notation,[17] where the first, second, and fourth integers represent the number of quanta in the ν_1, ν_2, and ν_3 vibrational modes, respectively. The third integer is the angular momentum, and the fifth integer designates the Fermi level. Band center locations were estimated using anharmonic coupled oscillators to represent the different modes. Harmonic oscillator scaling was used for the band strengths of the hot bands. This amounts to scaling the bands by a factor of $(n_3 + 1)$ relative to the fundamental. More accurate hot band intensities can be used if they are available. When $E_{max} = 25{,}000$ cm^{-1}, there are 10,000 hot bands (corresponding to 2×10^6 rotational-vibration lines) that are necessary to accurately represent the spectral absorption coefficient up to 3500 K.

The use of scaled and shifted fundamental lines to represent hot bands is tantamount to assuming that vibrational-rotational coupling does not vary with vibrational energy. Consider the implications of this approximation for the 4.3-μm band of CO_2. At room temperature the fundamental band contributes ~92% of the integrated intensity. Since our approach includes the fundamental band without approximation, low-temperature emission calculations should be accurate to a few percent. The largest fractional errors encountered using our approximate lines occur at moderate temperatures, 500–1000 K, where the lower overtones and hot bands contribute a significant fraction of the total spectral intensity. At high temperatures the band intensity is spread over millions of overlapping lines, and so small errors in the approximate location of the lines are not significant. The error in using the approximate lines can be determined by comparing calculated absorption coefficients using the approximate lines and the more accurate HITRAN data base. The percent error in the 500-K absorption coefficient is plotted in Fig. 3 for spectral resolutions of 1 and 5 cm^{-1}. As expected, the errors are rather large at a 1 cm^{-1} resolution, reaching peak values of nearly ± 200%. Most of this error is due to the errors in the emission frequency of the approximate calculation. The 5-cm^{-1} resolution plot shows peak errors of roughly 20% in the absorption coefficient.

For a high-temperature comparison, the use of approximate lines can be compared with a more exact quantum mechanical

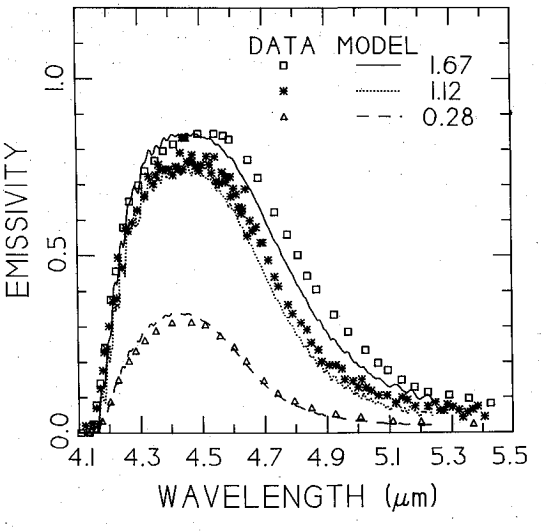

Fig. 6 Calculated and observed spectral emissivities from measurements of Ferriso et al. for three optical densities (atm cm). The calculations are shown as lines, observed data as symbols.

formulation developed by Bernstein et al.[22] In Fig. 4, the 5-cm^{-1} resolution CO_2 absorption coefficients for 3000 K determined using the present approach are compared with those determined using the more exact approach. The curves have very similar shapes and differ by less 10% throughout the band.

Validation of Radiation Transport Model

There have been several high-temperature experiments measuring the emissivity of CO_2 under a variety of optical densities. These experiments include shock tube[23] and flame experiments.[24,25] The most recent experiment was conducted by Coppalle and Vervisch.[24] They measured spectral absorptivity and emissivity of CO_2 produced in an oxygen-methane flame at 2900 K in the 4.3-μm spectral region. In Fig. 5, the calculated emissivities are compared with the experimental results for three optical densities of CO_2: 5.3, 1.43, and 0.5 cm · atm that correspond to path lengths of 21.2, 6.8, and 2.0 cm, respectively. The detailed inputs for our calculations are shown in Table 1. There is excellent agreement between our model and the experiments for the optically thin and thick cases. In the intermediate case, our model predicts approximately 20% more emissivity than observed in the experiments. Coppalle and Vervisch estimated their errors to be ± 150 K for the temperature and 5% on the concentration measurements. Using these errors, we calculated the maximum and minimum emissivities at two frequencies; see Fig. 5. Clearly the experimental errors cannot account for the difference between the model and the experimental data for the intermediate optical density.

Another high-temperature emissivity measurement for the CO_2 4.3-μm band was performed by Ferriso et al.[25] These experiments include two emissivity measurements with optical densities that are similar to the intermediate case of Coppalle and Vervisch. Ferriso et al. measured the spectral emissivity for temperatures of 2850, 2650, and 3000 K for CO_2 optical densities (total pressure) of 1.12 (2 atm), 0.28 (1 atm), and 1.67 atm · cm (5 atm), respectively. The total pressures are higher, 2- or 5-atm pressure, compared with 1-atm pressure in the measurements of Coppalle and Vervisch, although for pressures above 0.5 atm the high-temperature emission of CO_2 has been shown to be pressure independent.[23] In Fig. 6, the three sets of data measured by Ferriso et al. are compared with our present model using the detailed inputs given in Table 2. The agreement between the model and the data is quite good for all measured optical densities. The calculations are low by less than 10%, which is comparable to the estimated uncertainties of the measurements. The intermediate optical density emissivity measurements by Coppalle and Vervisch appear to be inconsistent with the measurements of Ferriso et al. The model calculations predict emissivities that fall between the experimental results.

Table 2 Flame conditions for calculation

Optical density, atm · cm	Pressure, atm	Temperature, K	X_{CO_2}	X_{CO}	X_{H_2O}
0.28	1.0	2650	0.17	0.22	0.28
1.12	2.0	2850	0.24	0.18	0.35
1.67	5.0	3000	0.20	0.20	0.32

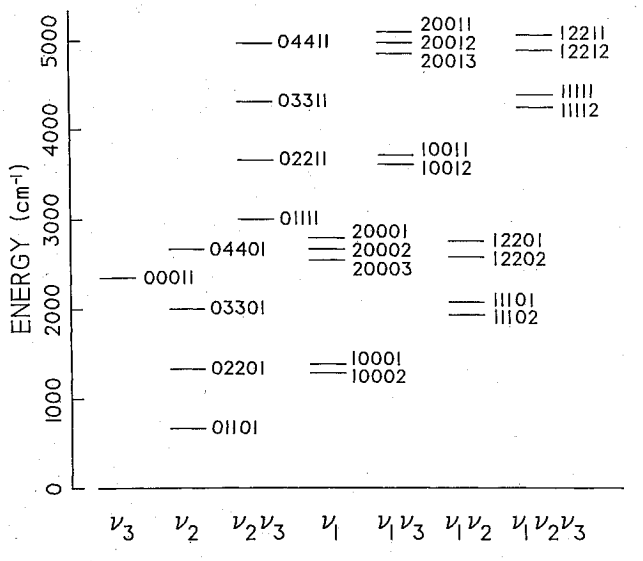

Fig. 7 Energy levels of the CO_2 vibrational states used in the chemical kinetics mechanism for radiation from the 2.7-, 4.3-, and 15-μm bands.

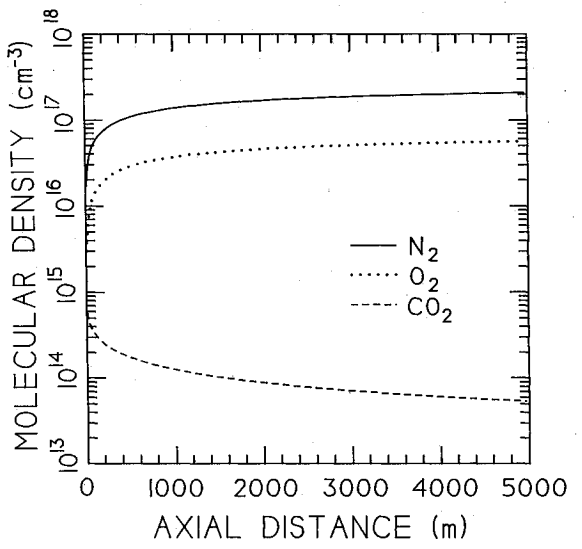

Fig. 8 Axial dependence of the major wake flowfield species, N_2 and O_2, and the dominant radiating species, CO_2, at 30.5 km.

Application to Re-Entry Vehicle Wakes

Molecular infrared radiation from the wake region of re-entry vehicles in the endosphere has only been studied assuming the vibrational temperatures are in equilibrium with the flow temperature. The justification for such an assumption has been that the collision rate is large enough to keep the vibrational and translational degrees of freedom in equilibrium. This section evaluates the equilibrium assumption by using the chemical-kinetics overlay model with a one-dimensional wake flowfield model. As a major contributor to IR radiation and a minor wake flow species, CO_2 is a good species to use for investigation of nonequilibrium effects. Furthermore, the spectroscopic data base and radiation transport model have been extensively validated for CO_2.

Vibrational Temperatures

The calculation of vibrational state populations requires that the vibrational energy transfer pathways for a given radiating species be understood well enough to establish the chemical-kinetics mechanism [Eq. (1)]. Furthermore, since populations are established by collisions between the radiating species and other flowfield species, the collisional excitation and deexcitation rate constants must also be known. The chemical kinetics involving vibrational energy transfer for various vibrational modes of CO_2 have been well studied to provide an understanding of the CO_2-N_2 laser system[26] and the energy

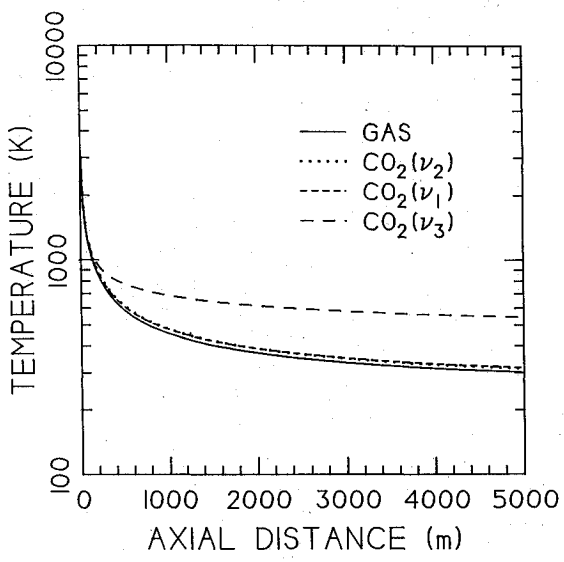

Fig. 9 Axial dependence of the flowfield gas-kinetic temperature and the vibrational temperatures of the ν_1, ν_2, and ν_3 fundamental bands of CO_2 at 30.5 km assuming initial vibrational temperatures in equilibrium with the flow.

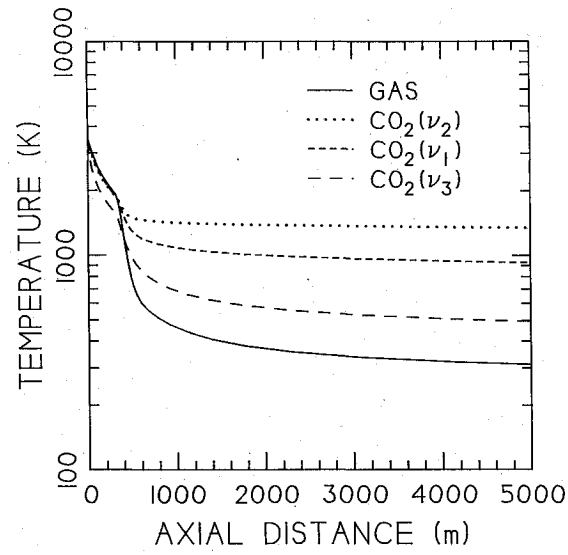

Fig. 10 Axial dependence of the flowfield gas-kinetic temperature and the vibrational temperatures of the ν_1, ν_2, and ν_3 fundamental bands of CO_2 at 57.9 km assuming initial vibrational temperatures in equilibrium with the flow.

budget of the upper atmosphere.[27] Even though most studies have focused on energy transfer involving CO_2 fundamental transitions, a reasonably realistic energy transfer mechanism can be constructed for vibrational states up to approximately 5000 cm^{-1}. The CO_2 energy levels necessary to reliably describe energy transfer among vibrational states below 5000 cm^{-1} are shown in Fig. 7. The notation for the vibrational states $(n_1n_2ln_3x)$ is standard HITRAN notation,[17] which was explained earlier.

Energy transfer for CO_2 can be more easily discussed by grouping the vibrational states together, where the individual states in each group are strongly coupled to each other due to the small energy difference between the states. For example, the groups illustrated in Fig. 7 are composed of combination states: $(022n_31 \leftrightarrow 100n_3x)$, $(033n_31 \leftrightarrow 111n_3x)$, and $(044n_31 \leftrightarrow 122n_3x \leftrightarrow 200n_3x)$ with $n_3 = 0, 1$. Although the states within a particular group are strongly coupled to each other via collisions, they are also coupled to other states by radiative relaxation, vibrational-translational (V→T) energy exchange with major flow species (N_2, O_2, and O), and vibrational-vibrational (V→V) energy exchange with N_2. The V→V energy exchange between CO_2 and N_2

$$CO_2(n_1n_2ln_3x) + N_2(0) \rightleftharpoons CO_2(n_1n_2ln_3 - 1x) + N_2(1) \quad (14)$$

is a near-resonant process and is the major contributor to the excitation of the ν_3 fundamental and combination bands. Emission at 4.3 μm involves the relaxation of the ν_3 manifold

$$CO_2(n_1n_2ln_3x) \rightarrow CO_2(n_1n_2ln_3 - 1x) + h\nu \quad (15)$$

The most important V→T energy transfer process involves the ν_2 manifold of states

$$CO_2(n_1n_2ln_3x) + M \rightleftharpoons CO_2(n_1n_2 - 1l - ln_3x) + M \quad (16)$$

where M represents N_2, O_2, and O. The V→T quenching of ν_2 by N_2 or O_2 is not nearly as efficient as the V→V transfer of ν_3 quanta with N_2. Relaxation of the ν_2 manifold of states produces 15-μm radiation.

The initial wake conditions are provided by a series of computer codes that treat the aerodynamic heating, ablation of the heatshield material, the shock structure, and the boundary-layer flowfield of the vehicle along a specified trajectory. The wake flowfield is computed assuming a quasi-one-dimensional laminar flow at the ambient pressure with finite rate chemistry. This algorithm has been successfully used in studies of wake radar cross sections.

The dependence of several molecular densities on downstream distance predicted by the one-dimensional wake flowfield code at an altitude of 30.5 km is shown in Fig. 8. The major species in the flow, N_2 and O_2, increase as a function of distance downstream due to the mixing of the flow with the ambient atmosphere, of which N_2 and O_2 are the major components. The CO_2 shows the expected decrease in density with downstream distance due to the expansion of the flow, which is also typical of all other ablation products in the flow. Similar behavior is predicted by the one-dimensional calculation at an altitude of 57.9 km, although the densities are approximately a factor of 30–40 lower than the densities at 30.5 km for N_2 and O_2. The density of CO_2 is roughly the same at 57.9 and 30.5 km.

A chemical-kinetics model for the CO_2 energy transfer in the wake flowfield has been constructed using the states shown in Fig. 7 and the important V→T and V→V energy transfer processes mentioned previously. Rate constants for V→T and V→V energy transfer among the lower vibrational states $(01101 \leftrightarrow 00001$, $02201 \leftrightarrow 1000x$, and $00011 \leftrightarrow 00001)$ have been measured in the laboratory.[26] Since there are no measurements for the energy transfer among combination states, rate constants for these processes have been scaled from those involving the lower lying vibrational states. The resulting rate equations are solved along the streamlines for the CO_2 and N_2 vibrational populations using the wake flowfield properties. The initial vibrational temperatures for the CO_2 and N_2 vibrational states were assumed to be in equilibrium at the initial wake temperature. It is assumed that the ambient atmosphere that mixes with the wake is vibrationally cold, i.e., the N_2 and O_2 species are in their ground vibrational states. The vibrational temperatures for the CO_2 ν_1 (10001), ν_2 (01101), and ν_3 (00011) fundamental bands and the one-dimensional wake flowfield gas temperature are shown in Figs. 9 and 10 for altitudes of 30.5 and 57.9 km, respectively. The vibrational temperature of the first excited state of N_2, which is not shown in these figures, is nearly equal to the CO_2 ν_3 fundamental temperature due to the very fast V→V energy exchange between CO_2 and N_2. In fact, the mixing of the vibrationally cold ambient N_2 with the flow tends to quench the CO_2 ν_3 funda-

mental vibrational state, resulting in a reduction of the vibrational temperature downstream. At 30.5 km, the excitation/de-excitation rate is large enough to maintain vibrational equilibrium with the flow temperature until a downstream distance of 200 m is reached. At this point, the vibrational temperatures of CO_2 ν_3 fundamental and vibrationally excited N_2 show a significant departure from equilibrium, whereas the remaining CO_2 vibrational states are in equilibrium with the gas temperature. Although there are enough collisions to keep the CO_2 ν_3 fundamental mode in equilibrium with N_2, there are not enough collisions to keep the N_2 vibrational states in equilibrium with the flow. The V→T rates for vibrational relaxation and excitation of N_2 are simply not very efficient at these flow densities. Vibrational nonequilibrium effects are even more dramatic at 57.9 km, where all of the CO_2 vibrational modes display significant nonequilibrium behavior at downstream distances greater than 400 m. The vibrational temperatures of ν_1 and ν_2 fundamentals are frozen at distances slightly greater than 400 m. This behavior is due to radiative relaxation (which is slow for ν_1 and ν_2 fundamentals), being the only mechanism for vibrational relaxation since the excitation/de-excitation rate is less significant. In contrast, the ν_3 fundamental temperature displays significant nonequilibrium behavior throughout the flowfield. At distances less than 400 m, the fundamental ν_3 temperature is less than the gas temperature, as the radiative relaxation rate is greater than the excitation/de-excitation collisional rate. As the wake continues to expand, the gas temperature rapidly decreases and there are not enough collisions to keep N_2 and CO_2 ν_3 fundamental in equilibrium with the flow. The ν_3 fundamental vibrational temperature decreases more rapidly with axial distance than the ν_1 and ν_2 fundamental vibrational temperatures, again due to the mixing of cold N_2 with the wake.

The calculation of the vibrational temperatures in the wake flow requires that an initial temperature be provided at the beginning of the flow. For the calculations of temperatures

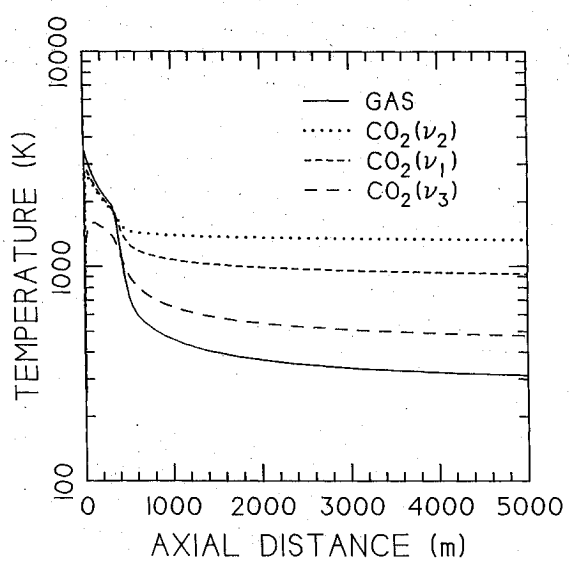

Fig. 11 Axial dependence of the flowfield gas-kinetic temperature and the vibrational temperatures of the ν_1, ν_2, and ν_3 fundamental bands of CO_2 at 57.9 km assuming initial vibrational temperatures in equilibrium with the ambient atmosphere.

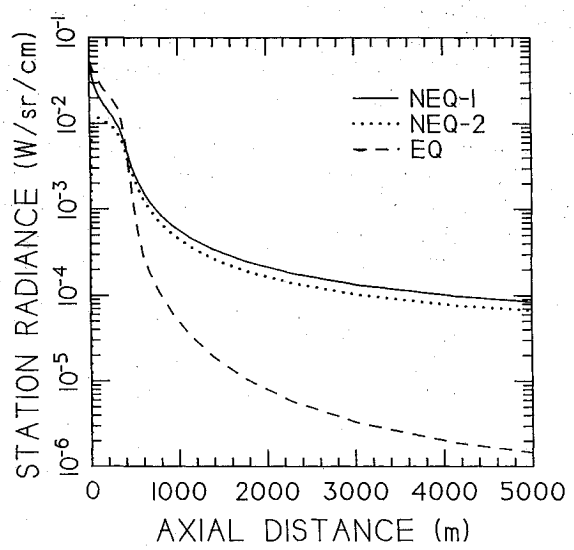

Fig. 13 Axial dependence of station radiance for the CO_2 4.3-μm band at 57.9 km under equilibrium and nonequilibrium conditions. The nonequilibrium calculations assume that initial vibrational temperatures are in equilibrium with the wake flowfield (NEQ.-1) and with the ambient atmosphere (NEQ.-2).

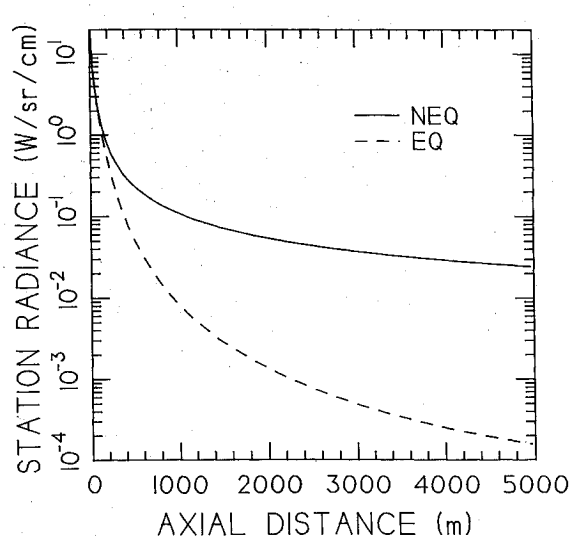

Fig. 12 Axial dependence of station radiance for the CO_2 4.3-μm band at 30.5 km under equilibrium and nonequilibrium conditions.

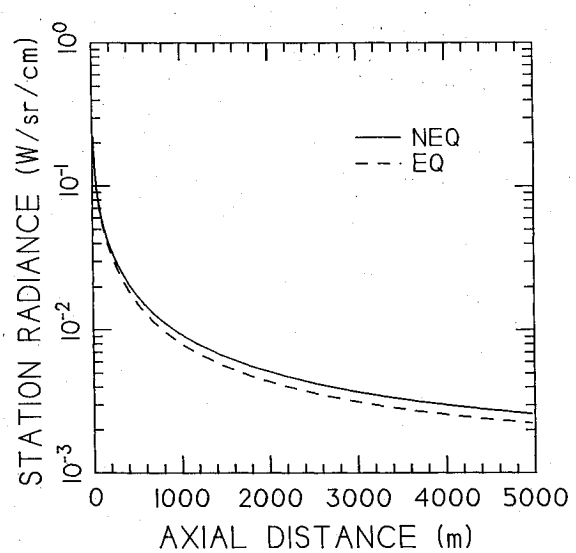

Fig. 14 Axial dependence of station radiance for the CO_2 15-μm band at 30.5 km under equilibrium and nonequilibrium conditions.

shown in Figs. 9 and 10, it was assumed that the start-line vibrational temperatures were at equilibrium at the flow temperature. At 30.5 km, it was shown than all CO_2 vibrational temperatures are in equilibrium with the flow up to 200 m downstream, indicating that the choice of initial vibrational temperatures is not important. However, at 57.9 km, the CO_2 ν_3 fundamental mode is in nonequilibrium throughout the flow, thus bringing into question the choice of initial vibrational temperatures. To assess the sensitivity of the vibrational temperatures to the initial conditions, CO_2 vibrational temperatures at 57.9 km were calculated using initial temperatures equal to the ambient atmospheric temperature of 260 K instead of the initial flow temperature of 3430 K. The resulting vibrational temperatures are shown in Fig. 11 and are to be contrasted with the temperatures shown in Fig. 10. As expected, there is relatively little effect on the ν_1 and ν_2 fundamental modes throughout the flow. At distances greater than 400 m, the ν_3 fundamental temperatures are also nearly independent of the initial temperature. However, at distances less than 400 m, ν_3 fundamental vibrational temperatures can vary

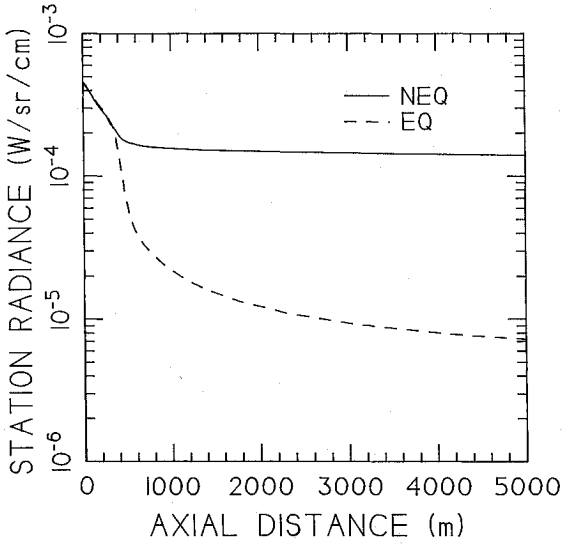

Fig. 15 Axial dependence of station radiance for the CO_2 15-μm band at 57.9 km under equilibrium and nonequilibrium conditions.

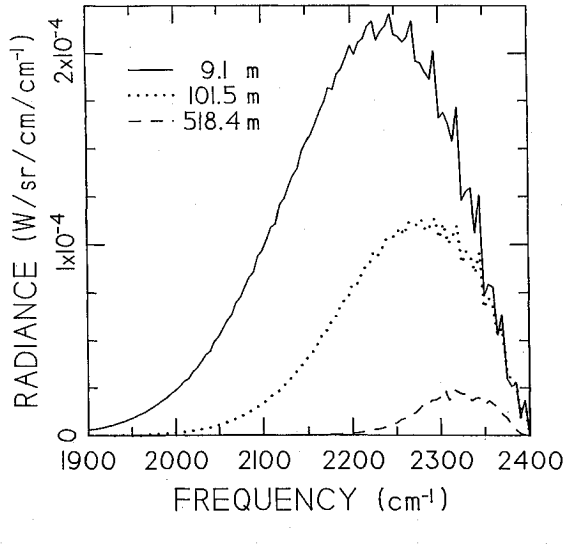

Fig. 16 Nonequilibrium calculation of the CO_2 4.3-μm spectral intensity at 57.9 km for several axial locations.

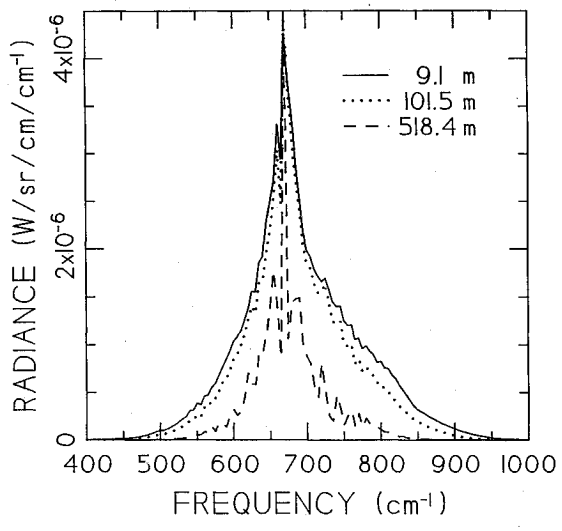

Fig. 17 Nonequilibrium calculation of the CO_2 15-μm spectral intensity at 57.9 km for several axial locations.

by 500–1500 K depending on the initial vibrational temperatures and location in the flowfield. Thus, a reliable prediction of the ν_3 fundamental vibrational temperature requires an understanding of the collisional history of the ν_3 mode before CO_2 enters the wake region.

Optical Signatures

The spectral radiance is calculated for broadside LOSs through the wake flowfield using the model described earlier. As demonstrated in Fig. 2, the radiance calculation for CO_2 4.3 μm at 3430 K requires vibrational states up to a maximum energy of 25,000 cm^{-1} (approximately 10,000 vibrational bands). Completely including all of these vibrational states in a chemical-kinetics mechanism is prohibitive because V→T and V→V energy transfer processes and associated rate constants must be specified for over 3000 vibrational states. Therefore, the CO_2 chemical-kinetics mechanism described previously (see Fig. 7) is used to determine the vibrational temperatures for three fundamental modes of CO_2, which are used to determine approximate vibrational temperatures for the hot bands. The first step in determining the approximate vibrational temperature is to decompose the upper state vibrational energy of the band into a sum of integer multiples of the n mode energies,

$$E_v = \sum_{n=1}^{3} \eta_n E_n \tag{17}$$

An approximate vibrational temperature for the state is then given by

$$T_v = E_v \left(\sum_{n=1}^{3} \frac{\eta_n E_n}{T_n} \right)^{-1} \tag{18}$$

The approximate vibrational temperature is used with each state energy to determine the population using a Boltzmann distribution.

The station radiance for CO_2 4.3-μm emission is shown in Figs. 12 and 13 for 30.5 and 57.9 km, respectively. At both altitudes considered, the radiation from the CO_2 4.3-μm band shows very significant downstream nonequilibrium effects. The decrease in nonequilibrium station radiance with increasing axial distance is simply due to the radiative relaxation of the vibrational modes. It is interesting that nonequilibrium effects do not always result in an increase in emission intensity. In particular, nonequilibrium effects will usually result in

a decrease of radiation if vibrational nonequilibrium exists from the beginning of the wake flowfield (see Figs. 10 and 11), since the vibrational temperatures are lower than, or equal to, the gas-kinetic temperature near the beginning of the flow. At 30.5 km, the total intensity integrated over 5000 m indicates that nonequilibrium effects result in 36% more total radiation than calculations based on equilibrium conditions. However, the same calculation at 57.9 km shows that nonequilibrium conditions produce 17–52% less radiation than equilibrium calculations, depending on the initial vibrational temperatures.

Figures 14 and 15 show the station radiance for CO_2 15-μm emission at 30.5 and 57.9 km, respectively. The 15-μm emission represents the extremes of equilibrium and nonequilibrium behavior. At 30.5 km, the emission is basically equilibrium, which was expected based on the discussion of vibrational temperatures. Significant nonequilibrium effects are indicated at 57.9 km, where the integrated nonequilibrium emission is 400% greater than the equilibrium calculation. In contrast to 4.3 μm, the 15-μm nonequilibrium station radiance is virtually constant for distances greater than 400 m due to the 0.6-s vibrational lifetime of the ν_2 manifold.

Spectral intensity calculations at 57.9 km for the CO_2 4.3-μm and 15-μm bands corresponding to several axial locations in the flowfield are shown in Figs. 16 and 17, respectively. As the axial distance increases, the magnitude and width of the spectral intensity decreases due to the decreasing vibrational temperatures. For the 4.3-μm band, the centroid of the band shifts to the blue (higher energy) due to fewer hot bands and rotational lines contributing to the band intensity. The shape of the 15-μm band does not change drastically, although the Q-branch of the fundamental transition (01101→00001) becomes a dominant spectral feature at axial locations greater than 500 m.

The calculation of the vibrational state populations and the 4.3-μm spectral signature for CO_2 requires roughly 1 min of computer time on a 20 MIPS Data General AViiON Server. The memory requirements vary with the number of axial stations, radial streamlines, and emission lines. The calculations shown here required about 3 megabytes of computer memory.

Conclusions

A chemical and thermodynamic nonequilibrium emission model has been applied to the problem of a high-velocity re-entry vehicle wake flow. The model consists of a "detailed" state-to-state treatment of T→V and V→V energy transfer processes occurring in a one-dimensional wake flowfield. The resulting nonequilibrium vibrational populations are used to determine vibrational temperatures for the fundamental modes of the molecular species. The mode vibrational temperatures are then used to determine approximate vibrational temperatures of hot bands that are used in a rapid, approximate radiative transfer algorithm to predict IR emission for fundamental and hot band emission at moderate spectral resolution (5 cm^{-1}), as well as spatially resolved emission for arbitrary spectral bandpasses. Significant nonequilibrium radiation effects are illustrated for CO_2 vibrational bands at 2.7, 4.3, and 15 μm at an altitude of 57.9 km and for the 4.3-μm band at 30.5 km.

The application of the nonequilibrium model to other species, such as CO, H_2O, and NO, present in the wake flowfield is currently being investigated. Detailed kinetic mechanisms, similar to that developed for CO_2, have been developed for energy transfer among CO, H_2O, and NO for vibrational states up to 5000 cm^{-1}. It appears that nonequilibrium behavior in the wake flowfield is widespread among many species produced during the ablation process.

Further application of the nonequilibrium model to more complicated species is currently limited by a lack of understanding of the kinetic energy transfer processes. The modeling of the nonequilibrium processes for many of these species does not appear possible at the present time. Based on the present work, it appears that equilibrium calculations should be capable of providing IR signatures within a factor of 2 of the more rigorous nonequilibrium results.

Acknowledgments

This work was performed for the Ballistic Missile Office (BMO) under Contract F04704-91-C-0008. The continuing interest and support of Jamie Kriebel of BMO and Tony Lin of TRW are appreciated. The authors are also grateful to Vreg Yousefian of Textron Defense Systems for supplying the one-dimensional wake flowfields.

References

[1]Arnold, J. O., Cooper, D. M., Park, C., and Prakash, S. G., "Line-by-Line Transport Calculations for Jupiter Entry Probes," *Entry Heating and Thermal Protection,* edited by W. G. Olstad, Vol. 69, Progress in Astronautics and Aeronautics, AIAA, New York, 1980, pp. 52–82.

[2]Park, C., "Calculation of Nonequilibrium Radiation in the Flight Regimes of Aeroassisted Orbital Transfer Vehicles," *Thermal Design of Aeroassisted Orbital Transfer Vehicles,* edited by H. F. Nelson, Vol. 96, Progress in Astronautics and Aeronautics, AIAA, New York, 1985, pp. 395–418.

[3]Gnoffo, P. A., Gupta, R. N., and Shinn, J. L., "Conservation Equations and Physical Models for Hypersonic Air Flows in Thermal and Chemical Nonequilibrium," NASA TP-2867, Nov. 1989.

[4]Dash, S. M., Pergament, H. S., Wolf, D. E., Sinha, N., Taylor, M. W., and Vaughn, M. E., Jr., "The JANNAF Standardized Plume Flowfield Code Version II (SPF-II)," U. S. Army Missile Command, CR-RD-SS-90-4, Redstone Arsenal, AL, July 1990.

[5]Bernstein, L. S., Sundberg, R. L., Zakin, M. R., Selby, J. E., Freeman, G. N., and Crow, D. R., "Nonequilibrium High-Altitude Rocket Plume Signature Model," *1990 Meeting of the Infrared Information Symposia Specialty Group on Targets, Backgrounds, and Discrimination,* Vol. 1, 213400-37-X(1), March 1990, pp. 47–68.

[6]Gear, C. W., *Numerical Initial Value Problems in Ordinary Differential Equations,* Prentice-Hall, Englewood Cliffs, NJ, 1971.

[7]Kee, R. J., Miller, J. A., and Jefferson, T. H., "CHEMKIN: Problem-Independent, Transportable, Fortran Chemical Kinetics Code Package," Sandia National Lab., SAND80-8003, Livermore, CA, March 1980.

[8]Plass, G. N., "Models for Spectral Band Absorption," *Journal of the Optical Society of America,* Vol. 48, No. 10, 1958, pp. 690–703.

[9]Bullitt, M. K., Bakshi, P. M., Picard, R. H., and Sharma, R. D., "Numerical and Analytical Study of High-Resolution Limb Spectral Radiance from Nonequilibrium Atmospheres," *Journal of Quantitative Spectroscopy and Radiative Transfer,* Vol. 34, No. 1, 1985, pp. 33–53.

[10]Fels, S. B., "Simple Strategies for Inclusion of Voigt Effects in Infrared Cooling Rate Calculations," *Applied Optics,* Vol. 18, No. 15, 1979, pp. 2634–2637.

[11]Zhu, X., "An Improved Voigt Line Approximation for the Calculations of Equivalent Width and Transmission," *Journal of Quantitative Spectroscopy and Radiative Transfer,* Vol. 39, No. 6, 1988, pp. 421–427.

[12]Rodgers, C. D., and Williams, A. P., "Integrated Absorption of a Spectral Line with the Voigt Profile," *Journal of Quantitative Spectroscopy and Radiative Transfer,* Vol. 14, No. 4, 1974, pp. 319–323.

[13]Oinas, V., "A New Method for the Rapid Calculation of Infrared Transmittances of Atmospheric Gases," *Journal of Quantitative Spectroscopy and Radiative Transfer,* Vol. 26, No. 4, 1981, pp. 381–383.

[14]Ludwig, C. B., Malkmus, W., Reardon, J. E., and Thompson, J. A. L., *Handbook of Infrared Radiation from Combustion Gases,* edited by R. Goulard and J. A. L. Thompson, NASA SP-3080, 1973, pp. 64–69.

[15]Curtis, A. R., "Discussion on A Statistical Model for Water-Vapour Absorption," *Quarterly Journal of the Royal Meteorological Society,* Vol. 78, No. 338, 1952, pp. 638–640.

[16]Godson, W. L., "The Computation of Infrared Transmission by Atmospheric Water Vapor," *Journal of Meteorology,* Vol. 12, No. 3, 1955, pp. 272–284.

[17]Rothman, L. S., Gamache, R. R., Goldman, A., Brown, L. R., Toth, R. A., Pickett, H. M., Poynter, R. L., Flaud, J.-M., Camy-Peyret, C., Barbe, A., Husson, N., Rinsland, C. P., and Smith, M. A.

H., "The HITRAN Database: 1986 Edition," *Applied Optics,* Vol. 26, No. 19, 1987, pp. 4058–4097.

[18]Bernstein, L. S., "Band Model Parameters for the Parallel Bands of Linear Triatomic Molecules-I. Theory," *Journal of Quantitative Spectroscopy and Radiative Transfer,* Vol. 23, No. 2, 1980, pp. 157–167.

[19]Pickett, H. M., Cohen, E. A., Brown, L. R., Rinsland, C. P., Smith, M. A. H., Malathy Devi, V., Goldman, A., Barbe, A., Carli, B., and Carlotti, M., "The Vibrational and Rotational Spectra of Ozone for the (0,1,0) and (0,2,0) States," *Journal of Molecular Spectroscopy,* Vol. 128, No. 1, 1988, pp. 151–171.

[20]Malkmus, W., "Infrared Emissivity of Carbon Dioxide (4.3 μ Band)," *Journal of the Optical Society of America,* Vol. 53, No. 8, 1963, pp. 951–961.

[21]Bernstein, L. S., "Development of a 10 cm^{-1} Resolution 6.3 μm H_2O Band Model," Spectral Sciences, Inc., SSI-TR-19, Burlington, MA, Jan. 1982.

[22]Bernstein, L. S., Robertson, D. C., and Conant, J. A., "Band Model Parameters for the 4.3 μm CO_2 Band from 200 to 3000 K—II. Prediction, Comparison to Experiment, and Application to Plume Emission-Absorption Calculations," *Journal of Quantitative Spectroscopy and Radiative Transfer,* Vol. 23, No. 2, 1980, pp. 169–185.

[23]Davies, W. O., "Emissivity of Carbon Dioxide at 4.3 μ," *Journal of the Optical Society of America,* Vol. 54, No. 4, 1964, pp. 467–471.

[24]Coppalle, A., and Vervisch, P., "Spectral Emissivity of the 4.3-μm CO_2 Band at High Temperature," *Journal of Quantitative Spectroscopy and Radiative Transfer,* Vol. 33, No. 5, 1985, pp. 465–473.

[25]Ferriso, C. C., Ludwig, C. B., and Acton, L., "Spectral-Emissivity Measurements of the 4.3-μ CO_2 Band Between 2650° and 3000°K," *Journal of the Optical Society of America,* Vol. 56, No. 2, 1966, pp. 171–173.

[26]Taylor, R. L., and Bitterman, S., "Survey of Vibrational Relaxation Data for Processes Important in the CO_2-N_2 Laser System," *Review of Modern Physics,* Vol. 41, No. 1, 1969, pp. 26–47.

[27]Dickinson, R. E., "Infrared Radiative Cooling in the Mesosphere and Lower Thermosphere," *Journal Atmospheric Terrestrial Physics,* Vol. 46, No. 11, 1984, pp. 995–1008.

Michael E. Tauber
Associate Editor